nature COMMUNICATIONS

ARTICLE

https://doi.org/10.1038/s41467-019-13769-z OPEN

Ultrasensitive negative capacitance phototransistors

Luqi Tu[1,2,6], Rongrong Cao[2,3,6], Xudong Wang[1], Yan Chen[1,2], Shuaiqin Wu[1,2], Fang Wang[1,2], Zhen Wang[1,2], Hong Shen[1], Tie Lin[1], Peng Zhou[4], Xiangjian Meng[1,2], Weida Hu[1,2,5*], Qi Liu[3*], Jianlu Wang[1,2,5*], Ming Liu[3] & Junhao Chu[1]

Sensitive photodetection is crucial for modern optoelectronic technology. Two-dimensional molybdenum disulfide (MoS_2) with unique crystal structure, and extraordinary electrical and optical properties is a promising candidate for ultrasensitive photodetection. Previously reported methods to improve the performance of MoS_2 photodetectors have focused on complex hybrid systems in which leakage paths and dark currents inevitably increase, thereby reducing the photodetectivity. Here, we report an ultrasensitive negative capacitance (NC) MoS_2 phototransistor with a layer of ferroelectric hafnium zirconium oxide film in the gate dielectric stack. The prototype photodetectors demonstrate a hysteresis-free ultra-steep subthreshold slope of 17.64 mV/dec and ultrahigh photodetectivity of 4.75×10^{14} cm $Hz^{1/2}$ W^{-1} at room temperature. The enhanced performance benefits from the combined action of the strong photogating effect induced by ferroelectric local electrostatic field and the voltage amplification based on ferroelectric NC effect. These results address the key challenges for MoS_2 photodetectors and offer inspiration for the development of other optoelectronic devices.

[1] State Key Laboratory of Infrared Physics, Shanghai Institute of Technical Physics, Chinese Academy of Sciences, 500 Yu Tian Road, Shanghai 200083, China. [2] University of Chinese Academy of Sciences, 19 Yuquan Road, 100049 Beijing, China. [3] Key Laboratory of Microelectronic Devices and Integrated Technology, Institute of Microelectronics, Chinese Academy of Sciences, 100029 Beijing, China. [4] State Key Laboratory of ASIC and System, School of Microelectronics, Fudan University, Shanghai 200433, China. [5] Hangzhou Institute for Advanced Study, University of Chinese Academy of Sciences, Hangzhou 310024, China. [6] These authors contributed equally: Luqi Tu, Rongrong Cao. *email: wdhu@mail.sitp.ac.cn; liuqi@ime.ac.cn; jlwang@mail.sitp.ac.cn

Sensitive, fast, and accurate detection of light is the foundation for the future optical communication, memory, sensing, imaging, and other optoelectronic applications. Photodetectors based on two-dimensional (2D) materials, such as graphene[1,2] and transition metal dichalcogenides[3–5], have emerged and drawn tremendous attention owing to their unique crystal structures, extraordinary electrical and optical properties, as well as the potential applications in ultrathin, transparent, and flexible optoelectronic devices[6,7]. The nature of a 2D optoelectronic material has largely determined the type and the working mechanism of its photodetectors[8–10]. Taking graphene as an example, as its gapless Dirac cone band structure results in ultrafast carrier recombination, graphene–metal junction and graphene p–n junction photodiodes are mainly exploited for separating photogenerated electrons and holes by the built-in electric field[1,11–13]. Graphene-based photodiodes with the characteristics of fast photoresponse but low photocurrent gain are hardly suitable for the room-temperature few-photon photodetection. On the contrary, molybdenum disulfide (MoS_2) phototransistors are promising for visible to near-infrared highly sensitive photodetection, due to its thickness-dependent band gap, high photoconductive gain, and high carrier mobility[14–20]. Back in 2013, the monolayer MoS_2 phototransistor was reported with responsivity (R) as high as 880 A W^{-1} at incident wavelength (λ) of 561 nm and power of 150 pW[21]. However, since its high responsivity is mainly attributed to trap states either in MoS_2 or at the interface between MoS_2 and SiO_2 substrate, the uncontrollability of trap states caused by material and interface defects, low detectivity, and slow photoresponse on the timescale of seconds seriously limit its practical applications.

Nowadays, nearly all researches on improving the performance of MoS_2 phototransistors focus on the hybrid systems combined with other material platforms such as graphene, quantum dots (QDs), perovskites, organic dye molecules, and surface plasmonic nanostructures[22]. For instance, the hybrid MoS_2-PbS QDs photodetector was reported with an ultrahigh responsivity of 6×10^5 A W^{-1}, yet large dark current of 0.26 μA, low detectivity, and high operating voltage[23]. Even though hybrid photodetectors using HgTe QDs demonstrate compelling sensitivity, the quality control of QDs and complicated preparation technology remain as the key challenges[24]. Besides, by incorporating organic dye molecules[25] or perovskites[26], MoS_2 photodetectors demonstrate enhanced optical absorption and responsivity, whereas it is inevitable to change the characteristic absorption spectrum and form leakage paths, resulting in large dark current and low detectivity. Furthermore, using high-mobility graphene as an expressway for carrier transport of phototransistors can only improve the performance of MoS_2 phototransistors to some extent, yet introducing undesirable complex interface and fabrication issues[27].

Here, an alternative approach is developing gate dielectric engineering in MoS_2 phototransistors. Ferroelectrics behave nonlinearly, which implies that phototransistors with a ferroelectric layer in the gate stack may have the ability to amplify the electrical response to optical signals. Ferroelectric hafnium zirconium oxide (HZO, $Hf_{1-x}Zr_xO_2$ with $x = 0.5$) thin film, with thickness scalability, complementary metal-oxide-semiconductor (CMOS) technology compatibility, and environmental friendliness, is thought as a kind of superior nonlinear gate dielectric layer to regulate optoelectronic characteristics of MoS_2 phototransistors. Recent researches have demonstrated the photogating effect in MoS_2 phototransistors, where trapped holes enable photogenerated electrons to circulate through an external circuit more than once leading to large photocurrent[20,28]. Besides, photogating effect can not only achieve the photoconductive gain but also lead to the threshold shift of phototransistors. Although the uncompensated dangling bonds or water molecules at the MoS_2/oxide interface contribute to trap states to a certain extent, the ferroelectric HZO gate dielectric layer dominates and enhances the photogating effect by trapping more holes in the ferroelectric local electrostatic field, yielding high photoconductive gain and large threshold shifts. Moreover, ferroelectric negative capacitance (NC) effect, that the capacitance of ferroelectrics is negative during the process of ferroelectric polarization switching, possesses the ability to accomplish voltage amplification and ultra-steep subthreshold slope (SS) in the phototransistor with a ferroelectric layer in its gate stack[29–34]. Therefore, MoS_2 phototransistors based on ferroelectric HZO films can efficiently amplify the change of the channel energy barrier induced by threshold shifts, resulting in that more electrons can go across the channel energy barrier and form large photocurrent. On the whole, ferroelectric HZO film is supposed to improve the performance of MoS_2 phototransistors through strengthening the photogating effect by trapping more holes in the ferroelectric local electrostatic field and amplifying the energy barrier drop caused by threshold shifts based on ferroelectric NC effect.

In this paper, we report an ultrasensitive NC MoS_2 phototransistor based on ferroelectric HZO thin film. In contrast to previously reported optimization strategies of MoS_2 photodetectors, ferroelectric HZO thin films in the gate dielectric stack can significantly enhance the photogating effect, suppress the dark current and improve the light to dark current ratio by ferroelectric local electrostatic field and ferroelectric NC effect, thereby yielding an ultrahigh photodetectivity while maintaining high responsivity and fast response. Experimentally, by the gate structure engineering and the semiconductor thickness scaling[35], MoS_2 phototransistors accomplish a hysteresis-free ultra-steep SS ($SS_{avg} = 45$ mV/dec, $SS_{min} = 17.64$ mV/dec). When illuminated, transfer characteristic curves shift to the left because of the strong photogating effect induced by ferroelectric local electrostatic field, yielding a change in phototransistor threshold voltage V_T (in the dark) to $V_T - \Delta V_T$ (under illumination). As a result of threshold shift, the drain current (I_{ds}) changes from I_{dark} to $I_{light} = I_{dark} + I_{ph}$ and follows $I_{ph} = I_{light} - I_{dark} = \int (dI_{ds}/dV_g) dV_T$, where I_{ph} is photocurrent, I_{dark} and I_{light} are the drain currents in the dark or under illumination. More specially, as dI_{ds}/dV_g is fully dependent on SS in the subthreshold region, ultra-steep SS induced by ferroelectric NC effect can efficiently increase photocurrent and improve detectivity[20]. Therefore, based on the combined action of the threshold shift and the ultra-steep SS, we demonstrate the prototype devices with ultrahigh detectivity of 4.7×10^{14} cm $Hz^{1/2}$ W^{-1} and high responsivity of 96.8 A W^{-1} under low operating voltages of $V_{ds} = 0.5$ V and $V_g = -1.6$ V at room temperature. These results address the key challenges for ultrasensitive MoS_2 photodetectors and are promising for the development of other photodetectors based on the photogating effect.

Results

Device structure and microscopic representation. Figure 1a, b is the structure schematic and the optical microscope photograph of the NC MoS_2 phototransistor, respectively. A metal-ferroelectric-insulator-semiconductor field effect transistor (MFISFET) was fabricated on a p-type silicon substrate, with TiN as the gate metal, HZO/Al_2O_3 as ferroelectric/insulator gate layers, multilayer MoS_2 as the channel semiconductor, and Cr/Au as the source and drain electrodes. The TiN layer is not only used as the back gate electrode but also as the substrate for growing high-quality ferroelectric HZO thin film by atomic layer deposition (ALD) process. The growth process of the ferroelectric HZO thin film is provided in "Methods" section, and the grazing-incident X-ray diffraction (GI-XRD) pattern of the ferroelectric HZO film

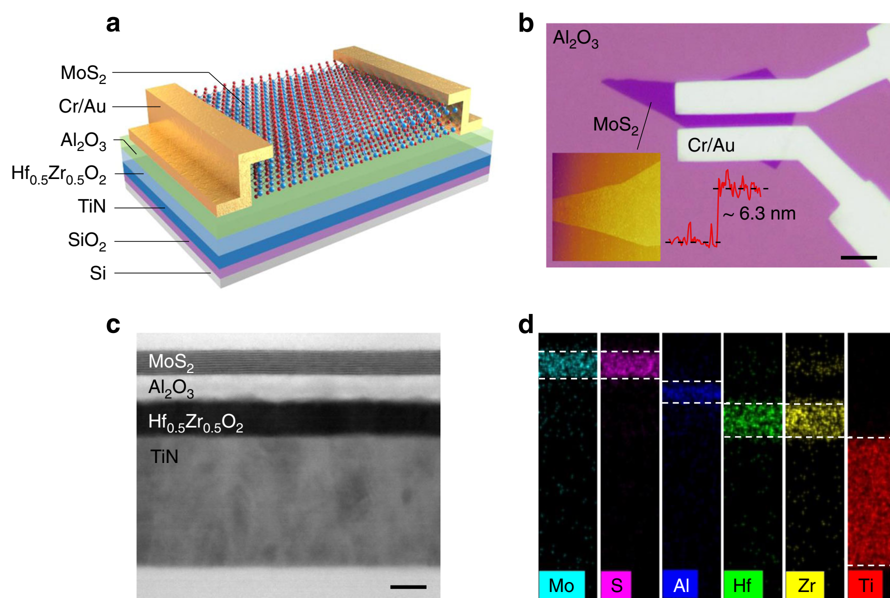

Fig. 1 Schematic of device structure and microscopic representation. a Structure schematic of MoS_2 phototransistors with the ferroelectric HZO thin film in the gate dielectric stack. **b** Optical microscope photograph of the device with MoS_2 channel length of 3 µm, width of 15 µm. Scale bar, 5 µm. The inset is the atomic force microscope (AFM) imaging of the multilayer MoS_2 flake, and the thickness of MoS_2 is measured as 6.3 nm (9 layers). **c** Transmission electron microscopy (TEM) imaging of the channel and gate of the device is in order with MoS_2/Al_2O_3/HZO/TiN layers. Interfaces of all layers are clear and flat. Scale bar, 10 nm. **d** Energy dispersive X-ray spectroscopy (EDS) elemental mapping of Mo, S, Al, Hf, Zr and Ti, corresponding to MoS_2/Al_2O_3/HZO/TiN layers in the TEM imaging.

is shown in Supplementary Fig. 1. Compared with conventional ferroelectrics, ferroelectric HZO thin film with thickness scalability, CMOS compatibility, and environmental friendliness is more applicable in future nanoscale electronic and optoelectronic devices. Besides, the amorphous Al_2O_3 layer plays an essential role in improving the quality of HZO/MoS_2 interface[36], including suppressing gate leakage current, achieving capacitance matching, and enhancing device stability[31,32]. As shown in Supplementary Fig. 2, metal-ferroelectric-semiconductor field effect transistors (MFSFETs) without the Al_2O_3 layer present inferior electrical properties. The inset in Fig. 1b is the atomic force microscope (AFM) imaging of a multilayer MoS_2 flake, and the thickness of MoS_2 is measured as 6.3 nm (nine layers) with the Raman spectrum of nine-layer MoS_2 shown in Supplementary Fig. 3[37]. Figure 1c, d is the cross-sectional transmission electron microscopy (TEM) imaging and the detailed energy dispersive X-ray spectrometry (EDS) elemental mapping of the channel and gate of the device. According to the TEM imaging, the thicknesses of MoS_2/Al_2O_3/HZO/TiN layers are 6.3/6/10/40 nm, and the interfaces of all layers are clear, flat, and free of impurities. Besides, the layered structure of the MoS_2 layer is discerned in Supplementary Fig. 4. Furthermore, the EDS analysis of Mo, S, Al, Hf, Zr, and Ti elements demonstrates that all elements are uniformly distributed and without inter-diffused.

Electrical properties of NC MoS_2 phototransistors. The ferroelectric properties of the HZO thin film, such as the hysteresis loop and the NC effect, play decisive roles in electrical and optoelectronic characteristics of NC phototransistors. Firstly, the solid blue line in Fig. 2a presents the hysteresis loop of the 10 nm-thick ferroelectric HZO thin film tested by a capacitor composed of Au/HZO/TiN layers (the maximum swept voltage of the *P-E* measurement is ±2.8 V, the frequency used is 1000 Hz, and the preset delay is 1000 ms). The hysteresis loop confirms the basic ferroelectric characteristics of HZO films with coercive field (E_c) of 1.5 MV cm^{-1} and remnant polarization (P_r) of 10 µC cm^{-2}, and the dashed red line fitted by the Landau–Khalatnikov (LK) equation $E = 2\alpha P + 4\beta P^3 + 6\gamma P^5$ shows the negative dP/dE[29,32]. Furthermore, the ferroelectric capacitance (C_{Fe}) is defined as the reciprocal of the second derivation of the potential energy (U) with respect to the charge (Q), written as $C_{Fe} = (d^2U/dQ^2)^{-1}$. The principle of the ferroelectric NC effect can be understood through device working mechanism schematics and ferroelectric double well energy landscapes[34] shown in Fig. 2b. At the beginning, the gate voltage of the device is negative and less than the threshold voltage, yielding the ferroelectric layer polarized downwards, the channel electrons depleted, and the device turned off. Then changing the gate voltage to the opposite, the ferroelectric layer is polarized upwards, the channel electrons are accumulated, and the device is turned on. In the process of mutual conversion of the above two ferroelectric polarization states, the ferroelectric is supposed to go across an energy barrier from one energy valley to another. According to the definition of the ferroelectric capacitance, this energy barrier is the ferroelectric NC region.

To get insight into the fundamental electrical characteristics of the NC MoS_2 phototransistors, Fig. 2c exhibits its equivalent capacitance schematic, where C_S, C_{ox}, and C_{Fe} represent the capacitance of MoS_2, Al_2O_3, and HZO layers, respectively. Notably, C_S also includes the stray capacitances of the source and drain shown in Supplementary Fig. 5. C_{ox}[38] and C_{Fe} can be calculated by the expression $C = \varepsilon S d^{-1}$, where ε, S, and d stand for the permittivity, area and thickness of dielectric layers, and the permittivity of the ferroelectric HZO thin film (ε_{Fe}) presented in Supplementary Fig. 6 is measured by the capacitor shown in Fig. 2a. Through a simple calculation, the relationship between SS and capacitances is obtained as $SS = [1 + C_S(C_{Fe}{}^{-1} + C_{ox}{}^{-1})] \times 60\ mV/dec = [1 - C_S(|C_{Fe}|^{-1} - C_{ox}{}^{-1})] \times 60\ mV/dec$. According to this expression, it is beyond doubt that capacitance matching is crucial to achieve sub-60 mV/dec ultra-steep SS. Based on an optimized 10 nm-thick HZO ferroelectric layer and an appropriate 6 nm-thick Al_2O_3 layer (according to the expression of SS,

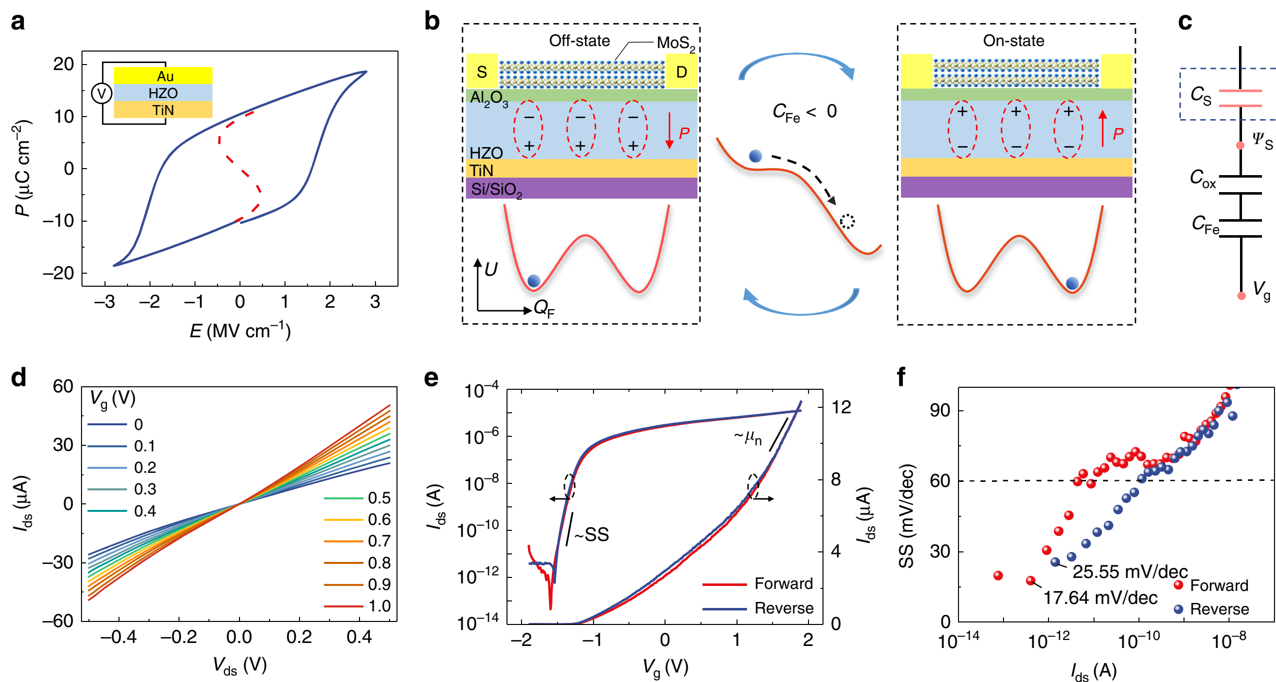

Fig. 2 Electrical measurement and results of the NC MoS_2 phototransistors. a Hysteresis loop (solid blue line) of the 10 nm-thick ferroelectric HZO thin film is measured by a capacitor composed of Au/HZO/TiN layers. The dashed red line fitted by the Landau–Khalatnikov (LK) equation $E = 2\alpha P + 4\beta P^3 + 6\gamma P^5$ shows negative dP/dE region. **b** Device working schematics and ferroelectric double well energy landscapes. During the process of ferroelectric polarization switching, the ferroelectric material is supposed to go across an energy barrier from one energy valley to another. This energy barrier is regarded as the ferroelectric NC region. **c** Equivalent capacitance schematic of the device, where C_S, C_{ox} and C_{Fe} represent the capacitance of MoS_2, Al_2O_3 and HZO layers, respectively. **d** Output characteristic (V_{ds}–I_{ds}) curves exhibit ohmic characteristics for all gate voltages. **e** Forward and reverse transfer characteristic (V_g–I_{ds}) curves under $V_{ds} = 0.1$ V are plotted in red and blue, respectively, and hysteresis between them is almost negligible. Electron mobility and SS are, respectively, extracted based on a linear scale (right axis) and a logarithmic scale (left axis). **f** SS is calculated according to the transfer characteristic curves, where the average value, the minimum values in forward and reverse (SS_{avg}, $SS_{min\text{-}for}$, and $SS_{min\text{-}rev}$) are 45, 17.64, and 25.55 mV/dec, respectively.

$|C_{Fe}|^{-1} - C_{ox}{}^{-1} > 0$ is a necessary condition for the sub-60 mV/dec ultra-steep SS), a series of thicknesses of MoS_2 are measured experimentally and the measurement results are shown in Supplementary Fig. 7. As the thickness of MoS_2 increases, that is the permittivity and capacitance of MoS_2 increase[35], the SS becomes steeper in accordance with the expression $SS = [1 - C_S(|C_{Fe}|^{-1} - C_{ox}{}^{-1})] \times 60$ mV/dec. Meanwhile, when the thickness of the MoS_2 is increased to 9.8 nm, a hysteresis about 0.16 V between forward and reverse V_g–I_{ds} curves is observed, which can be explained by the structural defects of MoS_2 or the stability condition of NCFETs. For one thing, the total number of structural defects increases with the thickness of MoS_2[39,40]. When V_g sweeps forward, charge traps in the MoS_2 layer inhibit the ferroelectric polarization switching by screening the electric field. After the traps have been neutralized, the ferroelectric polarization switches, leading to a large hysteresis and an abrupt jump in the reverse. For another, the stability condition of MFISFETs requires that the total gate-channel capacitance $C_{gc} = (C_S{}^{-1} + C_{ox}{}^{-1} + C_{Fe}{}^{-1})^{-1} = (C_S{}^{-1} + C_{ox}{}^{-1} - |C_{Fe}|^{-1})^{-1}$ has to be positive[29,31]. Increasing the thickness (capacitance) of MoS_2 may break the stability condition of the device, resulting in a large hysteresis in I_{ds}–V_g curves.

Through optimizing the thickness of MoS_2 in MFISFETs to 6.3 nm (nine layers), the MoS_2 phototransistor accomplishes hysteresis-free ultra-steep SS. The output characteristic (V_{ds}–I_{ds}) curves shown in Fig. 2d exhibit ohmic characteristics for all gate voltages. The output characteristic curves under larger drain voltages are presented in Supplementary Fig. 8. In Fig. 2e, the forward and reverse transfer characteristic (V_g–I_{ds}) curves (the swept voltage of V_g–I_{ds} measurements is ramped and the swept rate is 14.14 Hz corresponding to the number of data points per second) are plotted in red and blue, respectively, and the hysteresis between them is almost negligible (the gate leakage measurement is shown in Supplementary Fig. 9). For a linear scale (right axis), electron mobility (μ_n) is calculated as 54.2 cm^2 V^{-1} s^{-1} using the expression $\mu_n = (L/W)(S/C_{ins})V_{ds}{}^{-1}(dI_{ds}/dV_g)$, where C_{ins} stands for the total capacitance of gate insulators. For a logarithmic scale (left axis), SS calculated by the definition $SS = dV_g/d(\lg I_{ds})$ are presented in Fig. 2f, where the average value, the minimum value in forward and reverse (SS_{avg}, $SS_{min\text{-}for}$, and $SS_{min\text{-}rev}$) are 45, 17.64, and 25.55 mV/dec, respectively. The optimization of electrical characteristics paves the way for ultrasensitive photodetection of MoS_2 phototransistors working in the subthreshold region.

Mechanism of optical detection in NC MoS_2 phototransistors. For typical photodetection operation, the laser is incident perpendicularly to the device surface, and the spot covers the entire channel uniformly shown in Fig. 3a. The transfer characteristics of the phototransistors in the dark and under the illumination of various optical powers are presented in Fig. 3b. The changes in threshold voltage $V_{T,dark}$ (in the dark) to $V_{T,light} = V_T - \Delta V_T$ (under illumination) are observed in V_g–I_{ds} curves, and the threshold shift (ΔV_T) increases with the incident optical powers. As a result of the threshold shift, the channel current increases from I_{dark} to $I_{light} = I_{dark} + I_{ph}$, that is the photocurrent $I_{ph} = I_{light} - I_{dark} = \int (dI_{ds}/dV_g)dV_T$, where dI_{ds}/dV_g is fully dependent

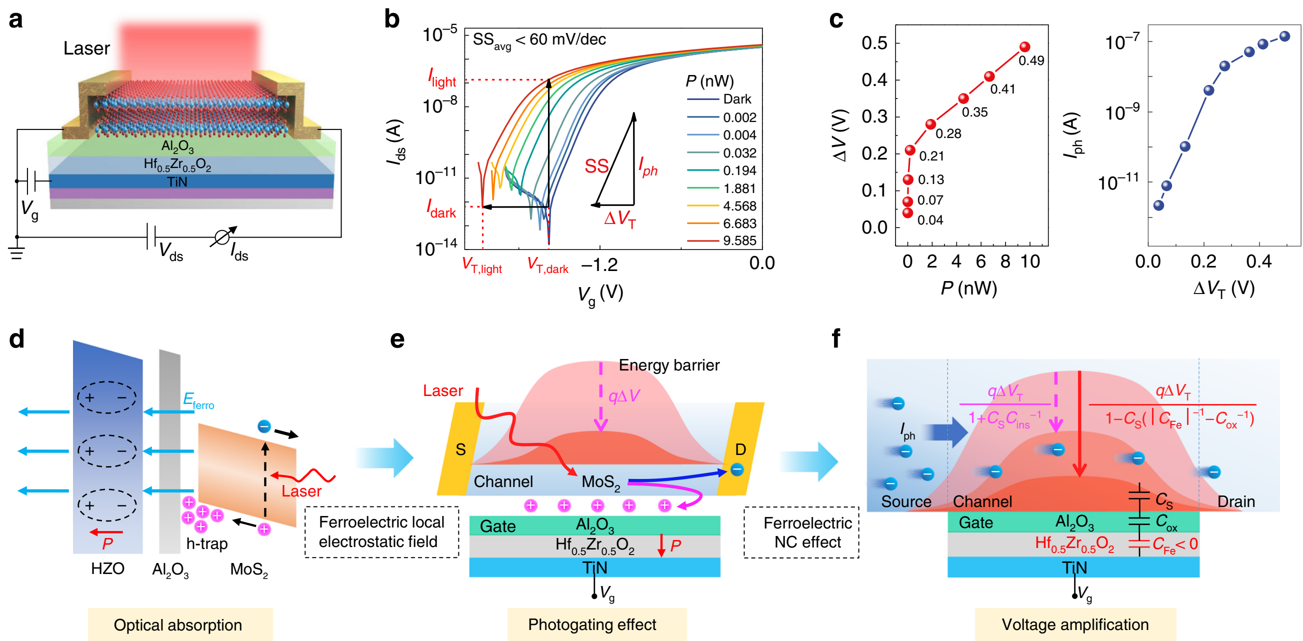

Fig. 3 Mechanism of ultrasensitive optical detection in the NC MoS_2 phototransistors. **a** Laser is incident perpendicularly to the device surface, and the spot covers the entire channel uniformly. **b** V_g–I_{ds} curves at $V_{ds} = 0.5$ V in the dark and under various incident light powers ($\lambda = 520$ nm). **c** Dependence of threshold shifts on the incident optical powers and dependence of photocurrent on threshold shifts are extracted from V_g–I_{ds} curves. **d** Under light illumination, enhanced light absorption can be achieved in multilayer MoS_2, generating electron-hole pairs efficiently by a strong light-matter interaction. **e** Photoexcited electrons are pulled toward the electrodes, while photoexcited holes are trapped in the gate stack due to the ferroelectric electrostatic local field, leading to strong photogating effect on the phototransistors. Photogating effect gives rise to a threshold shift as well as a reduction of the energy barrier in the channel ($q\Delta V$), so that more electrons can get over the energy barrier and forms photocurrent. **f** In generally, $q\Delta V = q\Delta V_T(1 + C_S C_{ins}^{-1})^{-1} < q\Delta V_T$ since the total capacitance of gate insulators (C_{ins}) is usually positive. However, MoS_2 NC phototransistors can break through this limitation and achieve a larger $q\Delta V = q\Delta V_T[1 - C_S(|C_{Fe}|^{-1} - C_{ox}^{-1})]^{-1} > q\Delta V_T$ based on the ferroelectric NC effect and capacitance matching conditions.

on SS in the subthreshold region. According to the definition of SS, with simple algebra the quantitative relationship among ΔV_T, I_{ph} and SS is obtained as $\lg(I_{light}/I_{dark}) = \lg I_{light} - \lg I_{dark} = \int SS^{-1} dV_T$, indicating that the large threshold shift and the ultra-steep SS work together to contribute to the ultrahigh light to dark current ratio and achieve ultrasensitive photodetection. Dependence of threshold shifts on incident optical powers and dependence of photocurrent on threshold shifts are extracted from V_g–I_{ds} curves and presented in Fig. 3c. Since the ability of the ferroelectric local electrostatic field to trap holes is gradually weakened as holes accumulated more and more in the gate stack, P–ΔV_T and ΔV_T–I_{ph} curves rise steeply for the incident optical power up to 0.2 nW and the threshold shift up to 0.21 V, respectively, and then gradually saturates.

To explore the mechanism of ultrasensitive photodetection, we focus on the working principles of optical absorption, photogating effect and voltage amplification in the device. Throughout the entire photodetection process, the operating voltages V_{ds} and V_g are set as constant, and the gate voltage equals to the threshold voltage of the device in the dark. For the dark state, the ferroelectric layer is polarized by the gate voltage, and the channel electrons are depleted by the ferroelectric electrostatic local field, therefore the phototransistor is turned off, and the dark current is suppressed to an extremely low level. Under light illumination, the enhanced light absorption can be achieved in multilayer MoS_2, generating electron-hole pairs efficiently by a strong light-matter interaction shown in Fig. 3d. Crucially, photoexcited electrons are pulled toward the external circuits, while photoexcited holes are trapped in the gate stack due to the ferroelectric electrostatic local field (E_{ferro}), leading to a strong photogating effect on the MoS_2 phototransistors. Furthermore, as presented in Fig. 3e, the photogating effect gives rise to a change of threshold voltage (ΔV_T) as well as a reduction of the energy barrier ($q\Delta V$) in the channel, so that more electrons can get over the energy barrier and form photocurrent. As shown in Fig. 3f, the channel energy barrier drop $q\Delta V = q\Delta V_T(1 + C_S C_{ins}^{-1})^{-1}$ is generally less than $q\Delta V_T$, since the total capacitance of gate insulators is usually positive. However, MoS_2 NC phototransistors can break through this limitation and achieve a larger $q\Delta V = q\Delta V_T[1 - C_S(|C_{Fe}|^{-1} - C_{ox}^{-1})]^{-1} > q\Delta V_T$ based on the ferroelectric NC effect and capacitance matching conditions. It means that ultrasensitive photodetection of NC MoS_2 phototransistors is fundamentally based on the combined action of the ferroelectric electrostatic local field and the ferroelectric NC effect.

Optoelectronic properties of NC MoS_2 phototransistors. To confirm the above mechanism, we next turn our attention to the photoresponse of the NC MoS_2 phototransistors. The optoelectronic measurements are performed under the illumination of a monochromatic light source with wavelength of 637 nm in a dark room at room temperature. Figure 4a presents the V_{ds}–I_{ds} curves in the dark and under various incident optical powers. To further evaluate the performance of the phototransistors, we extract the power dependence of photocurrent, light to dark current ratio, responsivity, external quantum efficiency (EQE) and detectivity from the V_{ds}–I_{ds} curves at $V_{ds} = 0.5$ V and $V_g = -1.6$ V. With the logarithmic scale, the photocurrent dotted in red and the light to dark current ratio dotted in blue increase with the incident optical powers and achieve maximum values as high as $I_{ph} = 5.22$ μA and $I_{light}/I_{dark} = 5.8 \times 10^7$ at $P_{eff} = 1116$ nW as shown in Fig. 4b. It is worth mentioning that P_{eff} is calculated by $P_{eff} = AP\pi^{-1}r^{-2}$, where A is the area of the sample, P is the actual laser output and r is the radius of the laser spot size. The responsivity $R = I_{ph}P_{eff}^{-1}$

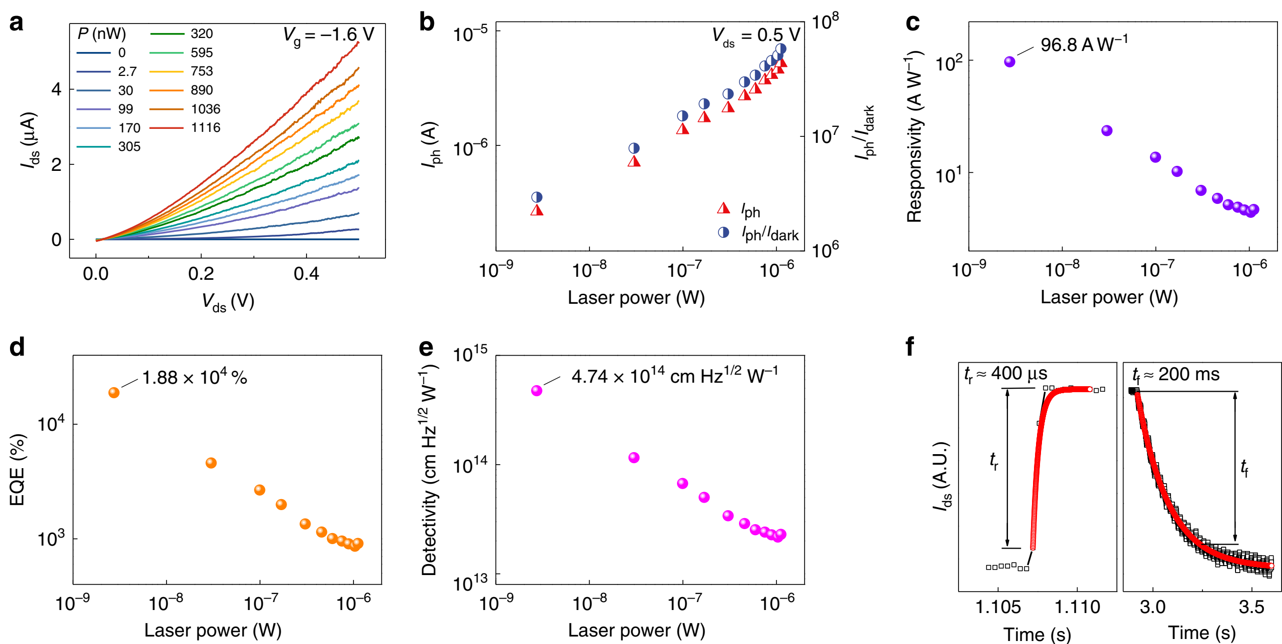

Fig. 4 Optoelectronic measurement and results of the NC MoS_2 phototransistors. a V_{ds}–I_{ds} curves in the dark and under various incident optical powers (λ = 637 nm). **b** With the logarithmic scale, the photocurrent (in red) and the light to dark current ratio (in blue) increase with the incident powers and achieve maximum values as high as $I_{ph} = 5.22$ μA and $I_{light}/I_{dark} = 5.8 \times 10^7$ at $P_{eff} = 1116$ nW. **c**, **d**, **e** Responsivity $R = I_{ph}P_{eff}{}^{-1}$, external quantum efficiency EQE $= hcR\lambda^{-1}e^{-1}$ and detectivity $D^* = RA^{1/2}(2eI_{dark})^{-1/2}$ show the same changing tendency with the incident powers, reaching the largest values of $R = 96.8$ A W^{-1}, EQE $= 1.88 \times 10^4$ %, $D^* = 4.75 \times 10^{14}$ cm Hz$^{1/2}$ W^{-1} at the lowest incident power of $P_{eff} = 2.7$ nW. **f** Rise (τ_r) and decay (τ_f) times of photocurrent are measured as 400 μs and 200 ms, respectively, and both the rise and decay curves (in black) are fitted well using exponential functions (in red).

indicates how much photocurrent can be produced by unit incident power on the photodetector, while the EQE defined as EQE $= hcR\lambda^{-1}e^{-1}$, is the ratio of the number of photoexcited carriers to the number of incident photons, where h is Planck constant, c is the speed of light and e is the electron charge. The responsivity and the EQE respectively plotted in Fig. 4c, d show the same changing tendency with the incident powers, reaching the largest values of $R = 96.8$ A W^{-1} and EQE $= 1.88 \times 10^4$ % at the lowest incident power of $P_{eff} = 2.7$ nW. The detectivity given by $D^* = RA^{1/2}(2eI_{dark})^{-1/2}$ is one of the most important parameters for photodetectors. The ultrahigh detectivity of $D^* = 4.75 \times 10^{14}$ cm Hz$^{1/2}$ W^{-1} is achieved at $P_{eff} = 2.7$ nW in Fig. 4e owing to the ultrahigh light to dark current ratio. Moreover, rise (τ_r) and decay (τ_f) times of photocurrent are measured as 400 μs and 200 ms, respectively, and both the rise and decay curves (in black) are fitted well using exponential functions (in red) shown in Fig. 4f.

We have also reviewed methods to improve the performance of MoS_2 phototransistors based on previously reported researches and this work. As one kind of the most investigated 2D material-based photodetectors, optimization strategies and detailed performance parameters of MoS_2 phototransistors are listed in Supplementary Table 1 to provide ideas for further exploration of other 2D optoelectronic semiconductors and their photodetectors[41–62]. There are four kinds of strategies regarding methods, including surface plasmon enhancement, charge-transfer assistance, impurity/energy band engineering of MoS_2, and gate engineering. Among these methods, charge-transfer-assisted hybrid systems combined with other material platforms such as graphene, QDs, perovskites and organic molecules are the most extensively studied strategy recently. The hybrid phototransistors present enhanced optical absorption and responsivity, whereas it is usually inevitable to introduce leakage paths, increase dark current, and slower response speed. As presented in Fig. 5, NC MoS_2 phototransistors based on gate dielectric engineering can circumvent these issues and demonstrate compelling performance with ultrahigh light to dark current ratio and detectivity, high responsivity and fast response, are promising for low-power and high-performance optoelectronic applications.

Discussion

In summary, based on the strategy of gate dielectric engineering, NC MoS_2 phototransistors with HZO ferroelectric thin films in the gate dielectric stack are proposed and fabricated. The prototype photodetectors demonstrate ultra-steep subthreshold slope of 17.64 mV/dec and ultrahigh detectivity of 4.75×10^{14} cm Hz$^{1/2}$ W^{-1} under $\lambda = 637$ nm and $P_{eff} = 2.7$ nW at room temperature, owing to the strong photogating effect of ferroelectric local electrostatic field and the ultra-steep SS induced by ferroelectric NC effect during the process of ferroelectric polarization switching. This high-performance MoS_2 photodetector should be a promising candidate for future optoelectronic applications and offer inspiration for the development of other optoelectronic devices. Furthermore, the gain mechanism relying on the combined action of the photogating and NC effects can be further exploited for the ultrasensitive few-photon detection technique and generally applicable to a large amount of low-dimensional semiconductors.

Methods

Fabrication of the multilayer MoS_2 phototransistor. A 40 nm-thick TiN layer was deposited by ion beam sputtering on 300 nm-thick SiO_2 grown on p-doped silicon substrates. The 10 nm-thick HZO thin film was grown on the TiN gate electrode by ALD process at 280 °C substrate temperature, and crystalized with a 60 s anneal at 500 °C in a nitrogen atmosphere. $Hf[N(C_2H_5)CH_3]_4$, $Zr[N(C_2H_5)CH_3]_4$ and H_2O were used as Hf precursor, Zr precursor and oxygen source, respectively. The Hf/Zr ratio was controlled by alternate deposition of one cycle HfO_2 and one cycle ZrO_2, which was confirmed by X-ray photoelectron spectroscopy (XPS). Then a 6 nm-thick Al_2O_3 layer was deposited on the HZO film by

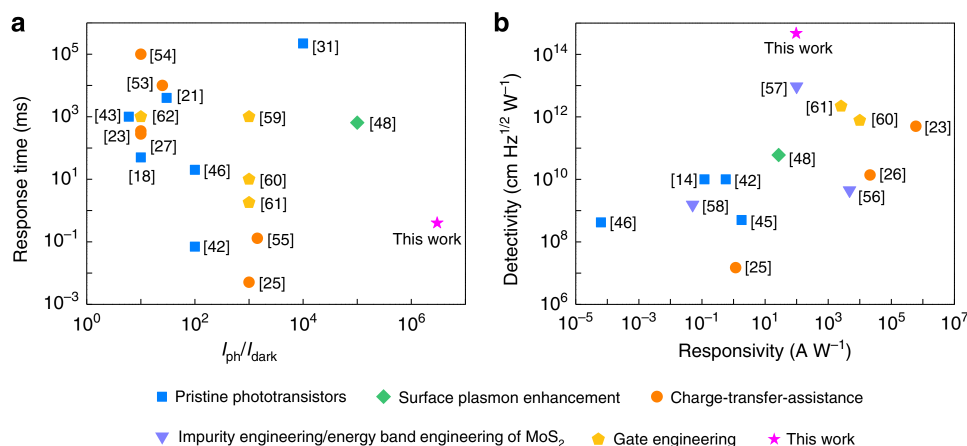

Fig. 5 Optimization strategy and performance summary of reported MoS_2 phototransistors. Optoelectronic properties (**a** response time and the ratio of photocurrent to dark current. **b** responsivity and detectivity) of NC MoS_2 phototransistors based on ferroelectric HZO gate dielectric engineering in this work outperform most of the previously reported MoS_2 phototransistors based on other strategies regarding methods, including surface plasmon enhancement, charge-transfer assistance and impurity/energy band engineering of MoS_2.

electron beam evaporation. Multilayer MoS_2 nano-sheets were mechanically exfoliated from bulk MoS_2 crystals and mounted on the Al_2O_3 layer. Finally, the source (S) and drain (D) metal electrodes were fabricated using electron-beam lithography, thermal evaporation of Cr/Au films (15 nm / 45 nm) and lift-off.

Polarization of the ferroelectric HZO Film. In MoS_2 NC phototransistors, the source electrode is connected to ground, and the polarization state of the ferroelectric HZO film in the gate stake is controlled by the gate voltage V_g, specific as follows. For the electrical measurement, taking Fig. 2e as an example, during the I_{ds}–V_g measurement (I_g–V_g is measured simultaneously and the results are shown in Supplementary Fig. 9), the source electrode is connected to ground, the drain voltage is constant ($V_{ds} = 0.1$ V), and the gate voltage sweeps forward (V_g is from −1.9 to 1.9 V) and then reverse (from 1.9 to −1.9 V). As V_g sweeps forward, the ferroelectric polarization switches from downward to upward, the channel electrons are gradually accumulated and the device is turned on. As V_g sweeps reverse, the ferroelectric polarization switches from upward to downward, the channel electrons are gradually depleted and the device is turned off. For the optoelectronic measurement, taking Fig. 4a as an example, the source electrode is connected to ground, the operating voltages V_{ds} and V_g are set as constant, and specially the gate voltage equals to the threshold voltage of the dark state ($V_g = V_{T,dark} = -1.6$ V), yielding that the ferroelectric layer is polarized downwards and the dark current is suppressed to an extremely low level.

Measurement of electrical and optoelectronic properties. The electrical and optoelectronic measurement were carried out with a Lake Shore probe station and a Keysight B1500A semiconductor device analyzer under ambient conditions at room temperature. The photoresponse was tested under illumination of 520 nm/637 nm monochromatic light sources in a dark room. The light source was generated, switched, and transmitted by a Thorlabs ITC4001 laser diode/temperature controller and a LM9LP fiber-pigtailed laser diode. The spot diameter of the light source on the device surface was 1 mm, and the multilayer MoS_2 nano-sheet of the device was positioned at the center of the spot. A high-speed Tektronix MDO3014 mixed domain oscilloscope was used to measure the time-resolved photoresponse.

Data availability

The data that support the plots within this paper and other findings of this study are available from the corresponding author upon reasonable request. The source data underlying Figs. 2a, d–f, 3b, c, 4a–f, 5a, b and Supplementary Figs. 1, 2b–d, 3, 6, 7b, c, e, f, 8 and 9 are provided as a Source Data file.

Received: 28 July 2019; Accepted: 22 November 2019;
Published online: 03 January 2020

References

1. Mak, K. F., Ju, L., Wang, F. & Heinz, T. F. Optical spectroscopy of graphene: from the far infrared to the ultraviolet. *Solid State Commun.* **152**, 1341–1349 (2012).
2. Bonaccorso, F., Sun, Z., Hasan, T. & Ferrari, A. C. Graphene photonics and optoelectronics. *Nat. Photonics* **4**, 611 (2010).
3. Mak, K. F. & Shan, J. Photonics and optoelectronics of 2D semiconductor transition metal dichalcogenides. *Nat. Photonics* **10**, 216 (2016).
4. Chhowalla, M. et al. The chemistry of two-dimensional layered transition metal dichalcogenide nanosheets. *Nat. Chem.* **5**, 263 (2013).
5. Wong, J. et al. High photovoltaic quantum efficiency in ultrathin van der Waals heterostructures. *ACS Nano* **11**, 7230–7240 (2017).
6. Xie, C. & Yan, F. Flexible photodetectors based on novel functional materials. *Small* **13**, 1701822 (2017).
7. Long, M., Wang, P., Fang, H. & Hu, W. Progress, challenges, and opportunities for 2D material based photodetectors. *Adv. Funct. Mater.* **29**, 1803807 (2019).
8. Brar, V. W., Sherrott, M. C. & Jariwala, D. Emerging photonic architectures in two-dimensional opto-electronics. *Chem. Soc. Rev.* **47**, 6824–6844 (2018).
9. Buscema, M. et al. Photocurrent generation with two-dimensional van der Waals semiconductors. *Chem. Soc. Rev.* **44**, 3691–3718 (2015).
10. Liu, Y. et al. Van der Waals heterostructures and devices. *Nat. Rev. Mater.* **1**, 16042 (2016).
11. Xia, F., Mueller, T., Lin, Y. M., Valdes-Garcia, A. & Avouris, P. Ultrafast graphene photodetector. *Nat. Nanotechnol.* **4**, 839 (2009).
12. Mueller, T., Xia, F. & Avouris, P. Graphene photodetectors for high-speed optical communications. *Nat. Photonics* **4**, 297 (2010).
13. Gabor, N. M. et al. Hot carrier-assisted intrinsic photoresponse in graphene. *Science* **334**, 648–652 (2011).
14. Choi, W. et al. High-detectivity multilayer MoS_2 phototransistors with spectral response from ultraviolet to infrared. *Adv. Mater.* **24**, 5832–5836 (2012).
15. Yoon, Y., Ganapathi, K. & Salahuddin, S. How good can monolayer MoS_2 transistors be? *Nano Lett.* **11**, 3768–3773 (2011).
16. Lee, H. S. et al. MoS_2 nanosheet phototransistors with thickness-modulated optical energy gap. *Nano Lett.* **12**, 3695–3700 (2012).
17. Conley, H. J. et al. Bandgap engineering of strained monolayer and bilayer MoS_2. *Nano Lett.* **13**, 3626–3630 (2013).
18. Yin, Z. et al. Single-layer MoS_2 phototransistors. *ACS Nano* **6**, 74–80 (2011).
19. Radisavljevic, B., Radenovic, A., Brivio, J., Giacometti, V. & Kis, A. Single-layer MoS_2 transistors. *Nat. Nanotechnol.* **6**, 147 (2011).
20. Furchi, M. M., Polyushkin, D. K., Pospischil, A. & Mueller, T. Mechanisms of photoconductivity in atomically thin MoS_2. *Nano Lett.* **14**, 6165–6170 (2014).
21. Lopez-Sanchez, O., Lembke, D., Kayci, M., Radenovic, A. & Kis, A. Ultrasensitive photodetectors based on monolayer MoS_2. *Nat. Nanotechnol.* **8**, 497 (2013).
22. Wu, C. C. et al. Elucidating the photoresponse of ultrathin MoS_2 field-effect transistors by scanning photocurrent microscopy. *J. Phys. Chem. Lett.* **4**, 2508–2513 (2013).
23. Kufer, D. et al. Hybrid 2D-0D MoS_2-PbS quantum dot photodetectors. *Adv. Mater.* **27**, 176–180 (2015).
24. Huo, N., Gupta, S. & Konstantatos, G. MoS_2-HgTe quantum dot hybrid photodetectors beyond 2 µm. *Adv. Mater.* **29**, 1606576 (2017).
25. Yu, S. H. et al. Dye-sensitized MoS_2 photodetector with enhanced spectral photoresponse. *ACS Nano* **8**, 8285–8291 (2014).
26. Kang, D. H. et al. An ultrahigh-performance photodetector based on a perovskite-transition-metal-dichalcogenide hybrid structure. *Adv. Mater.* **28**, 7799–7806 (2016).
27. Xu, H. et al. High responsivity and gate tunable graphene-MoS_2 hybrid phototransistor. *Small* **10**, 2300–2306 (2014).

28. Fang, H. & Hu, W. Photogating in low dimensional photodetectors. *Adv. Sci.* **4**, 1700323 (2017).
29. Salahuddin, S. & Datta, S. Use of negative capacitance to provide voltage amplification for low power nanoscale devices. *Nano Lett.* **8**, 405–410 (2008).
30. McGuire, F. A. et al. Sustained sub-60 mV/decade switching via the negative capacitance effect in MoS_2 transistors. *Nano Lett.* **17**, 4801–4806 (2017).
31. Nourbakhsh, A. et al. Subthreshold swing improvement in MoS_2 transistors by the negative-capacitance effect in a ferroelectric Al-doped-HfO_2/HfO_2 gate dielectric stack. *Nanoscale* **9**, 6122–6127 (2017).
32. Si, M. et al. Steep-slope hysteresis-free negative capacitance MoS_2 transistors. *Nat. Nanotechnol.* **13**, 24 (2018).
33. Catalan, G., Jiménez, D. & Gruverman, A. Ferroelectrics: Negative capacitance detected. *Nat. Mater.* **14**, 137 (2015).
34. Khan, A. I. et al. Negative capacitance in a ferroelectric capacitor. *Nat. Mater.* **14**, 182 (2015).
35. Cheiwchanchamnangij, T. & Lambrecht, W. R. Quasiparticle band structure calculation of monolayer, bilayer, and bulk MoS_2. *Phys. Rev. B* **85**, 205302 (2012).
36. Zou, X. et al. Interface engineering for high-performance top-gated MoS_2 field-effect transistors. *Adv. Mater.* **26**, 6255–6261 (2014).
37. Li, H. et al. From bulk to monolayer MoS_2: evolution of Raman scattering. *Adv. Funct. Mater.* **22**, 1385–1390 (2012).
38. Birey, H. Thickness dependence of the dielectric constant and resistance of Al_2O_3 films. *J. Appl. Phys.* **48**, 5209–5212 (1977).
39. Lu, C. P. et al. Bandgap, mid-gap states, and gating effects in MoS_2. *Nano Lett.* **14**, 4628–4633 (2014).
40. Zhou, W. et al. Intrinsic structural defects in monolayer molybdenum disulfide. *Nano Lett.* **13**, 2615–2622 (2013).
41. Zhang, W. et al. High-gain phototransistors based on a CVD MoS_2 monolayer. *Adv. Mater.* **25**, 3456–3461 (2013).
42. Tsai, D. S. et al. Few-layer MoS_2 with high broadband photogain and fast optical switching for use in harsh environments. *ACS Nano* **7**, 3905–3911 (2013).
43. Perea-López, N. et al. CVD-grown monolayered MoS_2 as an effective photosensor operating at low-voltage. *2D Mater.* **1**, 011004 (2014).
44. Lu, J. et al. Improved photoelectrical properties of MoS_2 films after laser micromachining. *ACS Nano* **8**, 6334–6343 (2014).
45. Ling, Z. P. et al. Large-scale two-dimensional MoS_2 photodetectors by magnetron sputtering. *Opt. Express* **23**, 13580–13586 (2015).
46. Lee, Y. et al. Trap-induced photoresponse of solution-synthesized MoS_2. *Nanoscale* **8**, 9193–9200 (2016).
47. Miao, J. et al. Surface plasmon-enhanced photodetection in few layer MoS_2 phototransistors with Au nanostructure arrays. *Small* **11**, 2392–2398 (2015).
48. Lee, S., Park, J., Yun, Y., Lee, J. & Heo, J. Enhanced photoresponsivity of multilayer MoS_2 phototransistor using localized Au schottky junction formed by spherical-lens photolithography. *Adv. Mater. Interfaces* **6**, 1900053 (2019).
49. Schornbaum, J. et al. Epitaxial Growth of PbSe Quantum Dots on MoS_2 Nanosheets and their Near-Infrared Photoresponse. *Adv. Funct. Mater.* **24**, 5798–5806 (2014).
50. Chen, C. et al. Highly responsive MoS_2 photodetectors enhanced by graphene quantum dots. *Sci. Rep.* **5**, 11830 (2015).
51. Huang, Y. et al. Van der Waals coupled organic molecules with monolayer MoS_2 for fast response photodetectors with gate-tunable responsivity. *ACS Nano* **12**, 4062–4073 (2018).
52. Wang, Y. et al. Solution-processed MoS_2/organolead trihalide perovskite photodetectors. *Adv. Mater.* **29**, 1603995 (2017).
53. Roy, K. et al. Graphene-MoS_2 hybrid structures for multifunctional photoresponsive memory devices. *Nat. Nanotechnol.* **8**, 826 (2013).
54. Zhang, W. et al. Ultrahigh-gain photodetectors based on atomically thin graphene-MoS_2 heterostructures. *Sci. Rep.* **4**, 3826 (2014).
55. Li, X. et al. A self-powered graphene-MoS_2 hybrid phototransistor with fast response rate and high on-off ratio. *Carbon* **92**, 126–132 (2015).
56. Kang, D. H. et al. High-performance transition metal dichalcogenide photodetectors enhanced by self-assembled monolayer doping. *Adv. Funct. Mater.* **25**, 4219–4227 (2015).
57. Li, S. et al. Enhanced performance of a CVD MoS_2 photodetector by chemical in situ n-type doping. *ACS Appl. Mater. interfaces* **11**, 11636–11644 (2019).
58. Xie, Y. et al. Ultrabroadband MoS_2 photodetector with spectral response from 445 to 2717 nm. *Adv. Mater.* **29**, 1605972 (2017).
59. Kwon, J. et al. Giant photoamplification in indirect-bandgap multilayer MoS_2 phototransistors with local bottom-gate structures. *Adv. Mater.* **27**, 2224–2230 (2015).
60. Kufer, D. & Konstantatos, G. Highly sensitive, encapsulated MoS_2 photodetector with gate controllable gain and speed. *Nano Lett.* **15**, 7307–7313 (2015).
61. Wang, X. et al. Ultrasensitive and broadband MoS_2 photodetector driven by ferroelectrics. *Adv. Mater.* **27**, 6575–6581 (2015).
62. Pak, Y. et al. Enhanced Performance of MoS_2 Photodetectors by Inserting an ALD-Processed TiO_2 Interlayer. *Small* **14**, 1703176 (2018).

Acknowledgements

This work was partially supported by the Strategic Priority Research Program of Chinese Academy of Sciences (XDPB12). Major State Basic Research Development Program (Grant No. 2016YFA0203900), and Key Research Project of Frontier Sciences of Chinese Academy of Sciences (QYZDB-SSW-JSC016, QYZDY-SSW-JSC042). Natural Science Foundation of China (Grant Nos. 61574151, 61574152, 61722408, 61725505, 11734016, 61674158 and 61835012).

Author contributions

J.L.W. conceived and supervised the project. L.Q.T. and J.L.W. fabricated the devices and performed the electrical measurements. R.R.C. and Q.L. prepared the HZO film and performed the P-E measurements. L.Q.T., W.D.H. and Z.W. performed photoresponse characterizations. L.Q.T., J.L.W., X.D.W., Y.C., S.Q.W., F.W. and Z.W. performed the data analysis. H.S., T.L., P.Z., X.J.M., M.L. and J.H.C. assisted with data analysis and interpretation. L.Q.T., J.L.W. R.R.C., Q.L. and W.D.H. co-wrote the manuscript. All authors discussed the results and revised the manuscript.

Competing interests

The authors declare no competing interests.

Additional information

Supplementary information is available for this paper at https://doi.org/10.1038/s41467-019-13769-z.

Correspondence and requests for materials should be addressed to W.H., Q.L. or J.W.

Peer review information *Nature Communications* thanks the anonymous reviewer(s) for their contribution to the peer review of this work.

Reprints and permission information is available at http://www.nature.com/reprints

Publisher's note Springer Nature remains neutral with regard to jurisdictional claims in published maps and institutional affiliations.

Open Access This article is licensed under a Creative Commons Attribution 4.0 International License, which permits use, sharing, adaptation, distribution and reproduction in any medium or format, as long as you give appropriate credit to the original author(s) and the source, provide a link to the Creative Commons license, and indicate if changes were made. The images or other third party material in this article are included in the article's Creative Commons license, unless indicated otherwise in a credit line to the material. If material is not included in the article's Creative Commons license and your intended use is not permitted by statutory regulation or exceeds the permitted use, you will need to obtain permission directly from the copyright holder. To view a copy of this license, visit http://creativecommons.org/licenses/by/4.0/.

© The Author(s) 2020